A Wide-Range Transmission Line-Based Linear Displacement Sensor

Ademola A. Mustapha, *Member, IEEE*, Omar S. Hassan, Temesgen D. Ataro, *Student Member, IEEE*, Mohammed Saif Ur Rahman, and Mohamed A. Abou-Khousa, *Senior Member, IEEE*

***Abstract*—Accurate displacement measurement is critical for many applications. Recently, a variety of radio frequency-based linear displacement sensing techniques were introduced. However, the application of the previously proposed techniques was either not fully demonstrated toward realizing the sensor and/or they were limited in measurement range to less than 4 cm. This article introduces a fully characterized wide-range radio frequency-based contactless linear displacement sensor. The sensor consists of a short-circuited 50-Ω microstrip line and a movable current-sensing resonant probe. The probe accurately measures the sinusoidal magnetic field distribution along the short-circuited transmission line from a certain distance above it. The measured normalized field values are mapped to displacement using the inverse of the sinusoidal function in the postprocessing stage. The proposed technique is comprehensively validated using simulations and measurements of a compact sensor prototype operating at 727.5 MHz. Furthermore, the merits of the proposed sensor compared to the widely accepted linear variable differential transformer (LVDT) displacement transducer are highlighted here. The metrological characterization of the proposed sensor shows that it offers a very wide dynamic range of 68 mm with a standard deviation of the estimation error of less than 0.09 mm (0.13% of the full range). It is also demonstrated that the proposed sensor outperforms the commercial LVDT transducer in terms of overall displacement measurement accuracy. In general, the proposed sensor is scalable and has a theoretical dynamic range of λ/2 making it suitable for a wide range of applications.**

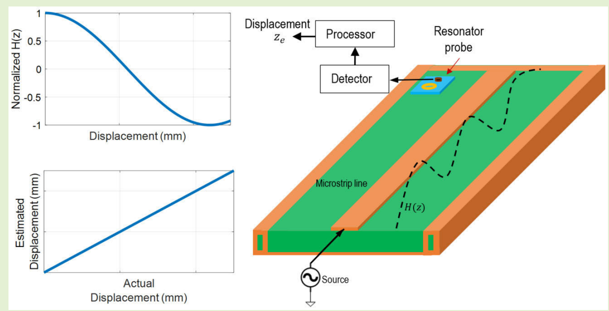

***Index Terms*—Current sensor, displacement sensor, magnetic field distribution, microstrip line, microwave, radio frequency, resonant loop, short circuited.**

I. Introduction

DISPLACEMENT sensors are vital in various industries and applications, such as robotics, industrial automation, aerospace, civil structures monitoring, and biomedical research [1], [2], [3], [4], [5], [6], [7], [8], [9], [10], [11], [12], [13], [14], [15]. Recent advancements have improved accuracy, resolution, integration capabilities, and dynamic measurement capabilities [9], [16], [17], [18], [19].

Manuscript received 1 June 2023; revised 18 June 2023; accepted 23 June 2023. Date of publication 6 July 2023; date of current version 15 August 2023. This work was supported in part by Khalifa University of Science and Technology, Abu Dhabi, UAE, under Award CIRA-2020-037; in part by the System-On-Chip Laboratory (SOCL); and in part by Khalifa University Space Technology and Innovation Center (KUSTIC). The associate editor coordinating the review of this article and approving it for publication was Dr. Kagan Topalli. *(Corresponding author: Ademola A. Mustapha.)*

The authors are with the Electrical Engineering and Computer Science Department, Khalifa University of Science and Technology, Abu Dhabi, United Arab Emirates (e-mail: ademola.mustapha@ku.ac.ae; omar.hassan@ku.ac.ae; 100058081@ku.ac.ae; mohammed.urrahman@ku.ac.ae; mohammed.aboukhousa@ku.ac.ae).

Digital Object Identifier 10.1109/JSEN.2023.3290912

Contact-based displacement sensors, such as potentiometers and LVDTs, continue to be widely used [20], [21], [22], [23], [24]. However, noncontact displacement sensors have gained popularity due to their nonintrusiveness and durability. These noncontact sensors employ various techniques to measure displacement without physical contact with the target object. Capacitive sensors rely on the changing capacitance with the distance between the sensor's electrodes and the target object [25], [26], while inductive sensors measure changes in inductance caused by the presence or movement of the target object [27], [28]. Eddy current-based sensors use electromagnetic induction to measure conductive target displacement by detecting impedance and phase changes due to interaction with the induced target's eddy currents [29]. Ultrasonic sensors estimate target displacement by emitting pulses and measuring the time it takes for the pulses to bounce back from the target [30]. Optical fiber-based sensors utilize coded disks and photodetectors to detect light patterns and determine precise target movement [7], [31]. Magnetic-based sensors utilize magnetic field variation to measure the position of a magnetic target, using sensors such as Hall effect sensors [32], [33], [34] or magnetoresistive sensors [35], [36], [37].

Another class of noncontact displacement sensors adopts a sensing principle between two noncontact parts, where one part may be attached to the target object [27], [28], [38], [39]. Most radio frequency-based displacement sensors, operating in the range of 3 kHz–300 GHz, with many operating in the microwave range (1–100 GHz) [40], [41], [42], [43], [44], [45], [46], [47], [48], [49], [50], belong to this class. They utilize radio frequency signals to measure and detect changes in displacement and have gained popularity due to high resolution, sensitivity, low-cost implementation potential, compact size, and robustness in harsh environments [40], [41], [42], [43], [44], [45], [46], [47], [48], [49], [50], [51]. These techniques have been extensively applied to implement linear displacement sensors involving measuring reflection coefficient [40], [41], [42], transmission coefficient [43], [44], [45], [46], phase of reflection or transmission coefficient [47], [48], [49], or phase change of radar signal [50].

However, some drawbacks have been identified in the previously reported radio frequency-based displacement sensors. One limitation is their narrow dynamic range, as demonstrated in a displacement sensor based on a patch-terminated coplanar waveguide (CPW) with a movable dielectric slab [40], yielding a maximum dynamic range of 7 mm. Also, a slotted transmission line and movable patch-based displacement sensor achieved a dynamic range of 3 mm [44]. The highest dynamic range reported so far is less than 40 mm, achieved through phase measurement [47], [49].

Furthermore, some microwave-based displacement sensing techniques require a wideband signal that covers the entire frequency range of the resonant frequency shift or transmission zero shift [40], [44], [45], which adds complexity to the hardware design and increases system costs. Single-frequency measurement techniques have been proposed [41], [42], [43], [46], [47], [48], [49], [50] to address these challenges, but their dynamic range is limited by the size of the resonator at microwave frequencies and unwanted amplitude variation. In addition, the tight coupling between the transmission line and the resonator leads to a fractional change in the resonant frequency due to loading, thereby reducing sensitivity at the single frequency of interest.

In general, the previously reported radio frequency-based displacement sensors have limitations in terms of dynamic range (<40 mm). In addition, many of the works focus on describing the variations in measured reflection or transmission parameters or resonant frequency shift with displacement without providing detailed information on how to obtain displacement in real applications. The metrological characterization of these sensing techniques, including quantifying displacement estimation error and uncertainty, is largely missing. Furthermore, the accuracy of these sensors relative to commercially available displacement sensors has not been thoroughly addressed in the reported works.

This article introduces a simple and contactless linear displacement sensing technique based on single-frequency radio frequency principles. Compared to previous radio frequency-based displacement sensors, it offers a wider dynamic range and a more robust design mechanism. The technique involves a fixed short-circuited transmission line and a movable resonant probe. The magnetic field distribution of the line is mapped by placing the probe at a distance above the transmission line, sensed through the coupling between the transmission line and the probe at the resonant frequency of the probe. The measurement range directly corresponds to the operating wavelength, making the lower radio frequency range advantageous for wider measurement ranges. The design of the transmission line and probe positioning ensures reduced susceptibility to noise and external electromagnetic field interference by maximizing coupling between the probe and the transmission line and, hence, the signal-to-noise ratio.

Unlike conventional magnetic sensors, the proposed sensor operates on a different principle. While magnetic sensors detect changes in static magnetic fields caused by magnetic materials, the proposed sensor generates a radio frequency (RF) magnetic field distribution around a nonmagnetic transmission line. It utilizes the wave behavior (standing wave), which is not observable in conventional magnetic sensors that utilize static magnetic fields. A nonmagnetic probe is then used to measure the field magnitude along the transmission line. Notably, the proposed sensor's sensing principle differs significantly from that of magnetic sensors, as it does not utilize magnets or magnetic materials/cores. The proposed sensor also has a higher dynamic range compared to magnetic sensors.

Furthermore, this article presents a low-cost implementation of the proposed sensor and provides a comprehensive characterization of its performance. To evaluate its performance, the proposed sensor is compared against a commercial linear variable differential transformer (LVDT) displacement transducer, widely used in the industry. The proposed sensor stands out as the first displacement sensor that utilizes the field distribution of a short-circuited transmission line instead of loading the line, and it also enables a simple calibration step for accurate displacement measurement. The primary novelty lies in the sensor's simple sensing mechanism, eliminating the need for complex geometrical structures found in current radio frequency designs. Importantly, this simplicity does not compromise accuracy or efficiency; in fact, the proposed sensor exhibits even greater accuracy compared to previous radio frequency works. Moreover, it provides an efficient method for precise displacement measurement, a feature that is largely absent in most reported radio frequency-based studies.

This article is structured as follows. Section II explains the underlying principle of operation of the proposed sensor. The design of each sensor component is described in Section III. Section IV presents the characterization results and sensitivity analysis. Section V presents the linear displacement measurement results. Section VI summarizes the sensor's performance metrics, comparing them with state-of-the-art and reported radio frequency-based linear displacement sensors. Finally, Section VII concludes this article.

II. Principle of Operation

The proposed sensor operates based on the principle of sensing the magnetic field distribution surrounding

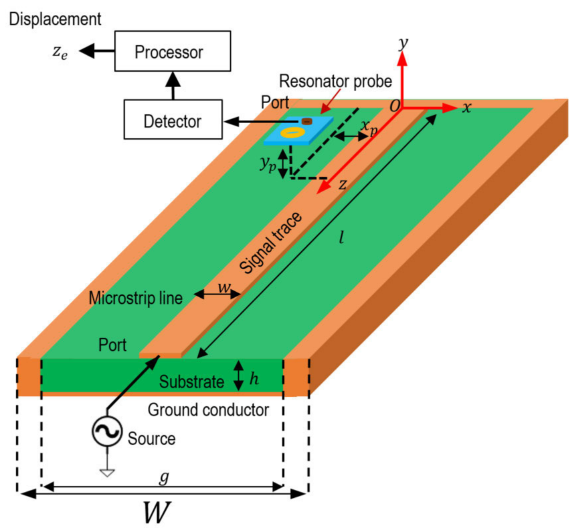

Fig. 1. Proposed sensor model comprising a source, short-circuited microstrip line, a resonator probe, a detector, and a processor.

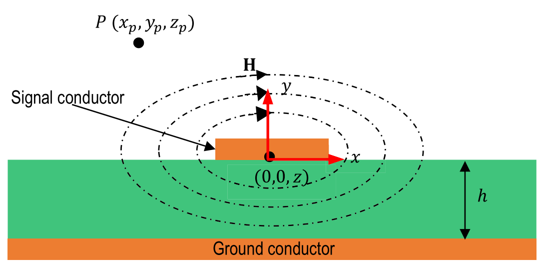

Fig. 2. Cross-sectional view of the microstrip line illustrating the magnetic field distribution around the line.

a short-terminated microstrip line, as shown in Fig. 1. This linear displacement sensor comprises two primary components: a fixed short-circuited 50-Ω microstrip line (signal trace) and a movable resonator probe. The transmission line is driven by a continuous-wave (CW) signal from a radio frequency source (oscillator) operating at frequency f_0. Due to the short termination at the end of the transmission line, a standing-wave pattern is established over its length. The longitudinal current standing-wave pattern exhibits a sinusoidal dependency on the position/displacement z relative to the location of the short, and it repeats periodically with a period equal to half the wavelength (λ_g) in the transmission line.

The current flowing through the microstrip line generates a magnetic field that surrounds the signal trace, as shown in the cross-sectional view of the microstrip line in Fig. 2. To measure one component of the magnetic field generated by the current on the trace, a current probe resonating at f_0 is utilized. This probe takes the form of a small loop loaded with a spiral resonator, making it specifically sensitive to the magnetic field component orthogonal to its plane [52]. The resonator probe is positioned at coordinate (x_p, y_p) as shown in Fig. 1, while it is free to move along the z-axis. The signal coupled from the transmission line to the probe positioned above it is proportional to the current at the specific z-coordinate.

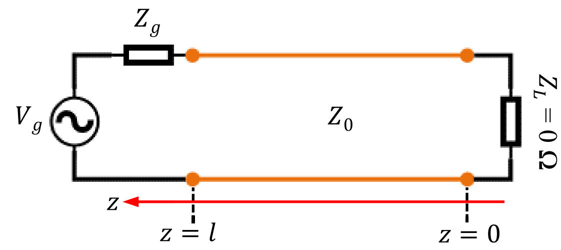

Fig. 3. Circuit representation of a terminated transmission line.

The coupling between the line and the probe can be measured by detecting the transmitted signal from port 1 to port 2 using a suitable detector. As the probe is moved along the z-axis, the magnetic field coupling between the transmission line and the probe aligns with the distribution of the standing-wave current along the shorted line. By considering the mathematical form of the current distribution as a function of the position z and analyzing the measured coupled signal, the probe's displacement from the short location can be estimated using the inverse function of the mathematical relationship. Importantly, the inverse mapping between the detected complex signal and the displacement is uniquely defined as long as the displacement remains within half the wavelength range. To facilitate this estimation process, a dedicated processor is employed to perform the necessary inversion calculations, thereby providing the estimated displacement of the probe relative to the short location.

The analysis of the current distribution surrounding the transmission line is further explored in the subsequent subsections, commencing with the examination of the surface current distribution.

A. Current Distribution Along the Transmission Line

The equivalent circuit representation of the terminated microstrip line of Fig. 1 is shown in Fig. 3. The line is terminated with $Z_L = 0\ \Omega$ at $z = 0$ and excited at position $z = l$ with a radio frequency source of impedance Z_g and voltage V_g. The current distribution along the short-circuited line is given as follows [53]:

$$I\,(z) = \frac{V_0^+}{Z_0}\left(e^{-\gamma z} + e^{\gamma z}\right) \tag{1}$$

where $V_0^+ e^{-\gamma z}$ is the incident voltage on the line at $z > 0$, Z_0 is the characteristic impedance of the line, and $\gamma = \alpha + j\beta$ is the complex propagation constant. The line is designed such that $Z_0 = Z_g = 50\ \Omega$.

Assuming that the loss in the transmission line is negligible, the following approximations can be applied:

$$\gamma \approx j\beta \text{ and } V_0^+ = (V_g/2)e^{-j\beta l}$$

where $\beta = 2\pi/\lambda_g$ is the phase constant. Hence, the current can be written as

$$I\,(z) = \frac{V_g}{Z_0}e^{-j\beta l}\cos\beta z. \tag{2}$$

B. Magnetic Field Distribution Around the Transmission Line

The magnetic field, **H**, around the microstrip line is shown in Fig. 2. To measure the magnetic field, a probe consisting of a loop loaded with a spiral resonator is placed above the transmission line at (x_p, y_p, z_p). The loop area lies in the xz plane. Hence, the resonant probe will be sensitive to the normal component of the H-field, namely, H_y. This component is zero above the center of the trace (i.e., at $x_p = 0$), and it is otherwise approximately proportional to the current in (2) when evaluated at $z = z_p$

$$H_y\left(x_p, y_p, z_p\right) \propto I\left(z_p\right) : x_p \neq 0. \tag{3}$$

This approximation holds well in practice as it will be demonstrated later.

It is evident from (2) and (3) that the field distribution is a sinusoidal function of displacement along the z-direction. This will be further demonstrated using simulations and measurements in the subsequent sections.

C. Displacement Estimation

From (2) and (3), the short-circuited transmission line of Fig. 1 can be used to estimate the displacement in one dimension. This is achieved by keeping the sensing probe at fixed x_p and y_p and moving it along the z-axis to estimate the displacement along that direction. The normalized response of the probe due to $H_y(x_p, y_p, z_p)$ can then be written as

$$h_n\left(z_p\right) = e^{j\phi_0} \cos\beta\left(z_p - z_0\right) \tag{4}$$

where the phase term ϕ_0 and the null offset z_0 are calibration factors that have been introduced to correct for the phase of the signal source and the probe offset from the reference position, respectively.

The normalized response h_n can be obtained by devising a highly sensitive probe to map the field distribution of the transmission line. The model parameters β, ϕ_0, and z_0 can be obtained from a calibration measurement of $h_n(z)$.

Therefore, the estimated displacement can be written as follows:

$$z_e = z_0 + Re\left(\frac{\cos^{-1}\left(h_n e^{-j\phi_0}\right)}{\beta}\right). \tag{5}$$

The inverse mapping between z_e and h_n exhibits a one-to-one relationship, ensuring a unique correspondence between the displacement and the magnetic field amplitude, as long as the displacement remains within the range of $\lambda_g/2$. This characteristic arises from the periodic nature of h_n, which repeats with a period of $(2\pi z_p/\lambda_g)$. Within a full range of λ_g, there exist four distinct values of z_e that yield the same magnitude of h_n. However, when the range is reduced to $\lambda_g/2$, only two z_e values correspond to a particular magnitude of h_n. To distinguish between these two values, the phase information of h_n at these positions can be considered. Notably, there is a phase difference of 180° between these two positions. Therefore, the theoretical dynamic range of the proposed sensor is limited to a maximum range of $0 < z_p < \lambda_g/2$.

The accuracy of the estimated displacement z_e depends on the accuracy of the normalized response h_n. Hence, to improve the sensor's accuracy, the sensor should be designed with minimal fluctuations during displacement measurement. This could be achieved by constructing a guiding structure for the sensor. The utilization of highly sensitive detectors will also result in more accurate estimations.

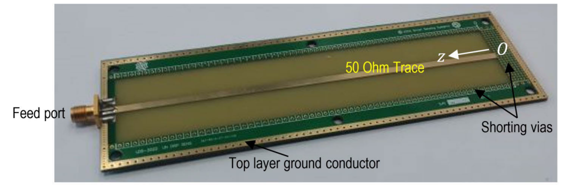

Fig. 4. Prototype of the short-circuited transmission line for the linear displacement sensor.

III. Sensor Design

To demonstrate the principle of operation described above, a prototype sensor operating at around 727.5 MHz was constructed and tested.

A. Design and Simulations of the Transmission Line

The short-circuited transmission line of Fig. 1 was designed on an FR-4 printed circuit board (PCB) with relative permittivity, $\varepsilon_r = 4.6$, loss tangent, $\tan\delta = 0.02$, and thickness, $h = 1.5$ mm. A photograph of the printed prototype is shown in Fig. 4. The width of the transmission line is $w \cong 2.8$ mm to yield 50-Ω characteristic impedance. The copper thickness for both the signal trace and the ground plane is $t = 0.035$ mm (1 oz). The width of the transmission line ground plane, $g \cong 30.5$ mm. However, the total width of the PCB was extended to $W \cong 51$ mm. This extension was necessary to accommodate the grounded guard located on the sides of the signal trace on the top layer, as well as the vias required to connect this guard to the ground plane on the bottom layer. The side ground trace guard helps in isolating the signal trace from external electromagnetic fields. One end of the signal trace is shorted to ground through the vias at $z = 0$, as shown in Fig. 4. Since the proposed sensor theoretically has a maximum dynamic range of $\lambda_g/2$ as explained in Section II-C, we set λ_g to 220 mm so that $\lambda_g/2$ is approximately 110 mm. This is about a factor of 3 higher than the dynamic range of the radio frequency-based displacement sensors reported in the literature. The total length of the transmission line was then chosen to be $l \cong 145$ mm to accommodate for the shorting vias and the feeding port. Considering the parameters of the transmission line given above, the effective relative permittivity of the transmission line is calculated to be $\varepsilon_{r,\mathrm{eff}} = 3.46$, resulting in a phase velocity of $0.5376c$ where $c = 3 \times 10^8$ m/s. This results in a design frequency of $f_0 = 733$ MHz for achieving a $\lambda_g/2$ dynamic range. The final operating frequency value depends on the precise tuning of the loop probe and it is given as 727.5 MHz in Section III-B.

The transmission line was simulated using the Dassault Systèmes Computer Simulation Technology (CST) Studio Suite [54] to investigate its field distribution and its reflection response. Also, the prototype was characterized in measurements using the Keysight N5225A vector network analyzer (VNA) to measure the reflection coefficient, S_{11}, at the input port of the microstrip line. A plot of the simulated and measured reflection coefficient of the short-circuited microstrip

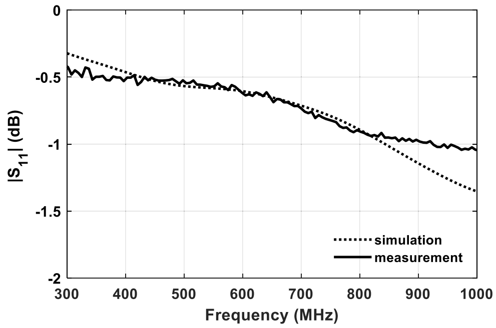

Fig. 5. Simulated and measured magnitude of the reflection coefficient at the input of the transmission line.

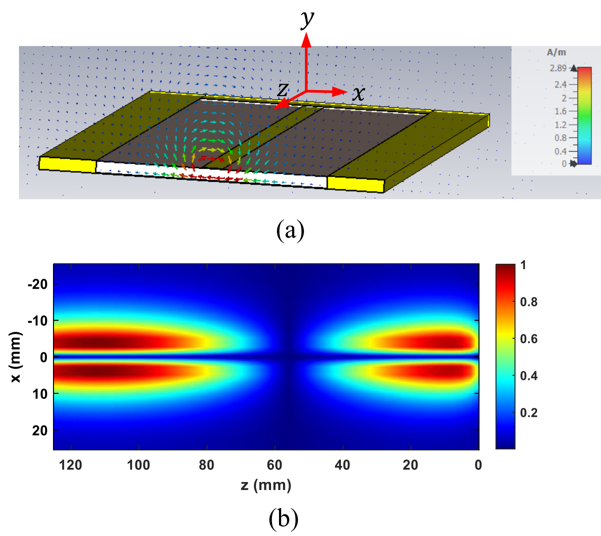

Fig. 6. Simulated magnetic field plot of the short-circuited transmission line (a) vector plot of $H(x, y)$ and (b) normalized absolute magnitude plot of $H_y(x, z)$ at an arbitrary y where $z = 0$ indicates the short-circuit position.

line is shown in Fig. 5. There is a very good match between the simulated and the measured magnitude responses of the reflection coefficient.

The CST field plot of the magnetic field, $\mathbf{H}$, of the short-circuited transmission line is shown in Fig. 6(a). The figure shows that the field strength reduces as the point P (cf. Fig. 2) is farther away from the surface of the microstrip. It also illustrates that the y-component of the field is zero ($H_y = 0$) at $x_p = 0$. Along the z-direction, Fig. 6(b) shows the H_y variation in the xz plane. The figure shows that the field strength is zero for all $x_p = 0$, and all $z_p \cong 56$ mm.

Fig. 7(a) presents a 1-D plot of the simulated normalized magnitude of $H_y(z)$, demonstrating that the response varies according to the cosine of the displacement from the shorted end of the transmission line. This observation aligns with the theoretical model described in (4). In addition, Fig. 7(b) shows the simulated phase response of $H_y(z)$, which exhibits two distinct phases with a phase transition occurring at $z_p \cong 56$ mm, the position of zero $|H_y(z)|$. Therefore, by combining the magnitude and the phase response, it is possible to accurately estimate the displacement within the range of $\lambda_g/2$ without any ambiguity.

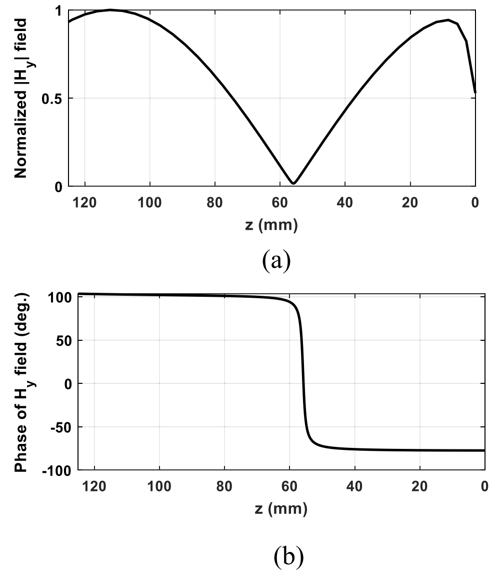

Fig. 7. Simulated magnetic field plot of the short-circuited transmission line: (a) normalized magnitude plot of $H_y(z)$ at an arbitrary x and y and (b) phase response plot of $H_y(z)$ at an arbitrary x and y.

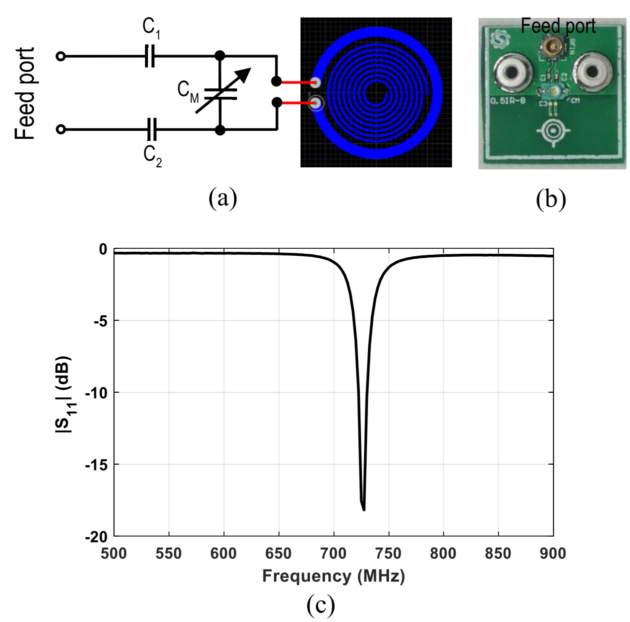

Fig. 8. (a) Schematic of the resonant probe with its matching network of capacitors, (b) printed prototype of the probe, and (c) measured reflection coefficient at the feed port of the resonant probe.

B. Design of the Resonant Probe

In order to be able to sense the magnetic field above the transmission line discussed in Section III-A, a magnetic field sensing probe was designed. The probe is a circular loop loaded with a circular spiral resonator. Fig. 8(a) shows the layout of the probe with its matching network. The top view of the printed prototype is shown in Fig. 8(b). The design of the probe is similar to the square loop probe of [52]. The spiral resonator comprises eight turns with an inner radius of 0.508 mm, a spiral width of 0.127 mm, and a spacing of 0.127 mm between each consecutive turn. Furthermore, the

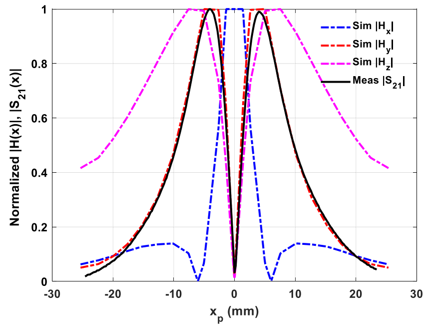

Fig. 9. Simulation and measurement results of the normalized H-field components at $y_p = 5$ mm and $z_p = 90$ mm. Results show a good correlation between the measured S_{21} and simulated H_y component.

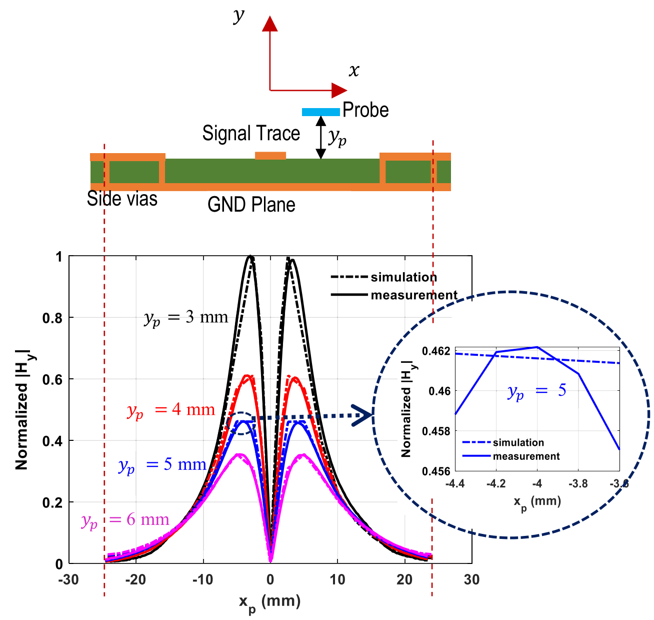

Fig. 10. Simulation and measurement results of the normalized $|H_y|$ at $z_p = 90$ mm and $y_p = 3, 4, 5$, and 6 mm, Inset: expanded x_p view at $x_p = -4$, $y_p = 5$ mm, and $z_p = 90$ mm.

spacing between the outermost turn of the resonator and the loop is 0.33 mm.

To match the probe to 50 Ω and tune its resonance frequency, fixed capacitors C_1 and C_2 along with shunt variable capacitor C_M were used. With $C_1 = C_2 = 1.5$ pF and C_M ranging from 1.8 to 4.5 pF, the probe was tuned to resonate at 727.5 MHz (close to the calculated design frequency of 733 MHz) as demonstrated in the measured reflection coefficient at the feed port of the probe shown in Fig. 8(c).

IV. Sensor Characterization and Sensitivity Analysis

In Section III, we presented the design and characterization of the individual components of the proposed sensor. In this section, we will focus on the coupling between the transmission line and the probe of the sensor. The objective of this section is to describe the sensitivity of the sensor in all three directions and optimize the probe placement for 1-D displacement measurement in the z-direction. In addition, we aim to demonstrate the correlation between the measurement results and both the simulation and theoretical model of the proposed sensor. Displacement estimation will be discussed in Section V.

During the sensor characterization and sensitivity analysis measurements, the probe was positioned above the transmission line as shown in Fig. 1 to observe the coupling between them. The coupling was measured through the complex transmission coefficient (S_{21}) between the transmission line input port and the probe port, with the magnetic field component H_y, being directly related to the measured transmission coefficient. A plot of the simulated H-field components at 727.5 MHz shown in Fig. 9 substantiates this fact. It is evident from the good match between the simulated $|H_y|$ and the measured $|S_{21}|$ results that the probe is accurately mapping the magnetic field component H_y.

In the first characterization and sensitivity analysis experiment, across-the-line scans were conducted by moving the probe along the x-axis (-24 to $+24$ mm) at an arbitrary z-coordinate of 90 mm with different heights (y-values) above the transmission line (3, 4, 5, and 6 mm). The specific z-coordinate (z_p) was not crucial as long as the measured signal was sufficiently strong, and it was important to avoid the null region around $z = 56.4$ mm [see the 2-D-image plot of Fig. 6(b) and the 1-D plot of Fig. 7(a)].

The measured $|S_{21}|$ results of Fig. 10 depict that the sensitivity of the sensor reduces with increasing distance y_p between the probe and transmission line. Furthermore, the results illustrate that the field magnitude exhibits symmetry in the cross section, peaking on both sides of the trace at approximately $x_p \approx \pm 4$ mm with a null (zero) value in the middle. These observations align with the expected behavior of the field around the microstrip trace [55], [56], [57]. The field decays toward the grounded guards on the sides. These findings are utilized to determine the optimal probe location, $x_p \approx \pm 4$ mm, where the coupling is maximized to enhance the signal-to-noise ratio and overall sensor sensitivity.

While the sensor exhibits its best response at $x_p \approx \pm 4$ mm, in practical situations, it is not necessary to differentiate between $x_p = +4$ mm and $x_p = -4$ mm. Either position can be used for displacement measurement. In addition, the inset of Fig. 10 depicts that any slight fluctuation of the probe within ± 0.4 mm would result in a maximum $|S_{21}|$ variation of 1.2%. This variation is further reduced to 0.3% if the probe is positioned such that $x_p = \pm 4 \pm 0.1$ mm. This requirement can be achieved by constructing a guiding structure that restricts the movement of the probe in the x-direction to a maximum of ± 0.1 mm. Furthermore, although the probe is most sensitive for smaller y_p values, the analysis of sensitivity along the transmission line response is required to determine an optimum value for y_p.

In the second characterization and sensitivity experiment, the probe was scanned from $z_p = 0$ (the position of the shorting vias) to $z_p = 125$ mm (just close to the feeding port) along the length of the transmission line at $x_p = -4$ mm and $y_p = 3, 4, 5$, and 6 mm each. Fig. 11 shows the measured and simulated $|H_y(z_p)|$ along the short-circuited transmission line. In general, the simulation and measurement results are in good agreement, especially for $y_p = 5$ mm

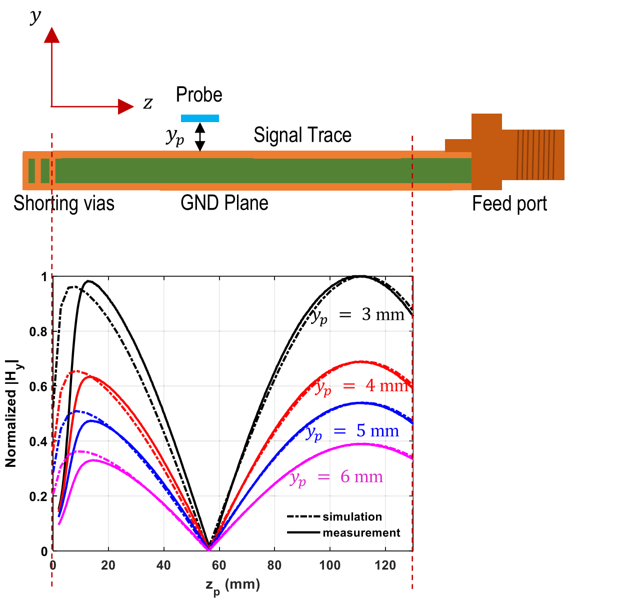

Fig. 11. Normalized $|H_y|$ along the transmission line at $x_p = -4$ mm and $y_p = 3, 4, 5$, and 6 mm.

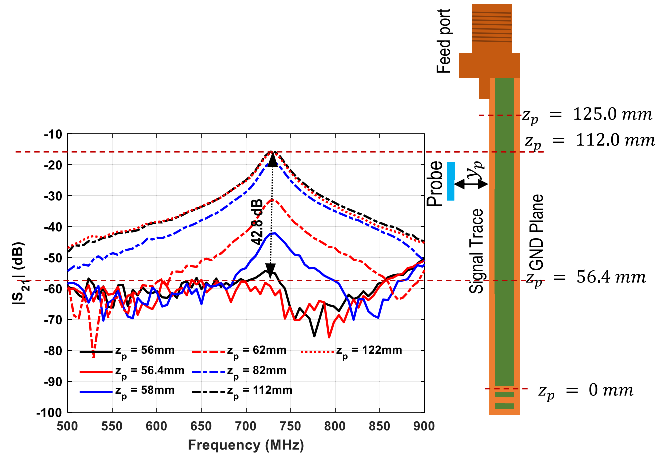

Fig. 12. Measured $|S_{21}|$ responses as the probe was moved from $z_p = 0$ to 125 mm. Results being displayed are only for the range $z_p = 56$ mm to $z_p = 125$ mm. Minimum $|S_{21}|$ of -58 dB is measured at $z_p = 56.4$ mm, while the maximum measured $|S_{21}|$ value of -15.2 dB occurs at $z_p = 112$ mm. In addition, the measured $|S_{21}|$ for $z_p < 56.4$ mm or $z_p > 112$ mm is also within the range of -15.2 to -58 dB.

and $y_p = 6$ mm. The discrepancy between the simulation and the measurement results for $y_p < 5$ mm is attributed to the probe-induced perturbation of the fields around the transmission line. Such perturbations could compromise the accuracy of the displacement measurements. Therefore, while determining the optimum vertical measurement distance, y_p, we considered two key factors: the sensitivity of the probe and its potential perturbation of the transmission line's field. Our selection was based on finding a vertical distance that maximizes probe sensitivity while minimizing any disruption to the field of the transmission line. Hence, the optimum value of y_p was chosen to be 5 mm where the probe senses a high signal, which enhances the overall system sensitivity, and yet, it does not cause significant perturbation. Hence, the optimum probe position in the xy plane is chosen to be $x_p = \pm 4$ mm and $y_p = 5$ mm.

The deviation of both the measurement and the numerical simulation results from the ideal sinusoidal response [i.e., the model in (3)] near the short location at $z_p = 0$ is primarily due to the current distribution in space around the grounded vias. At these locations, the current does not flow only along the z-axis but also down the vias to ground along the y-axis. Hence, it affects the magnetic field distribution as observed in other studies [57]. This deviation implies that the measurable dynamic range of the sensor is reduced from the maximum value of $0.5\lambda_g$ by approximately $0.12\lambda_g$.

The sensitivity of the displacement sensor to displacement along the z-direction was then analyzed by measuring $|S_{21}|$ as the probe is scanned along the z-direction at $x_p = -4$ mm and $y_p = 5$ mm. The measured result for a selected range of 56–125 mm is shown in Fig. 12. The measured results for the full range of 0–125 mm could not be displayed because the $|S_{21}|$ results for the range 0–56 mm are the same as for the range 56–112 mm.

As shown in Fig. 12, a maximum change of 42.8 dB in $|S_{21}|$ occurs when z_p varies from 56.4 mm (around standing-wave minimum) to 112.8 mm (around standing-wave maximum). The difference between the two positions represents a quarter wavelength of the guided wave at 727.5 MHz. The obtained measured signal range is adequately high for reliable signal detection with relatively inexpensive receivers as demonstrated later.

Since the $|S_{21}|$ response itself is not linear, the sensitivity of the sensor is a function of z_p and the specified displacement range. For instance, the sensitivity for a displacement range of $58 < z_p < 62$ mm is 2.75 dB/mm. Different values are obtained for different displacement ranges. Hence, the term "average" is used to calculate the average sensitivity of the sensor over its theoretical dynamic range of $\lambda_g/2$. The average sensitivity value at 727.5 MHz is therefore 0.76 dB/mm. This value is based on the $\lambda_g/4$ range of $56.4 < z_p < 112.8$ mm. Since the aim of this study is to design a wide dynamic range displacement sensor, maximizing the average sensitivity value is not practical considering the available detector circuits.

An essential observation from Fig. 12 is the true single-frequency operation of the proposed sensor. The maximum coupled signal occurs consistently at 727.5 MHz for every displacement, with a minimal random variation of only 1.25 MHz (0.17%). In addition, the resonant frequency of the probe exhibits a maximum variation of merely 0.25 MHz (0.03%). This negligible fractional change in frequency is attributed to the effective separation of the transmission line from the resonator, which prevents loading the resonator. This stands in contrast to most single-frequency resonator-based displacement sensors [41], [42], [46].

V. Displacement Measurement Results and Discussion

The displacement measurement capability of the sensor was verified by carrying out S-parameter measurements with the VNA using the measurement setup of Fig. 13. As discussed

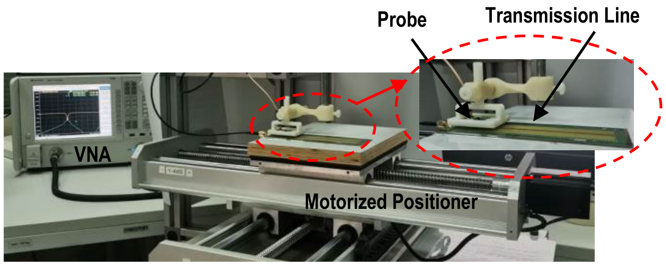

Fig. 13. Displacement measurement setup comprising the VNA, the motorized precision positioner, and the displacement sensor.

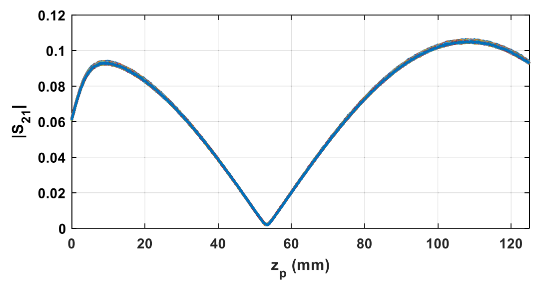

(a)

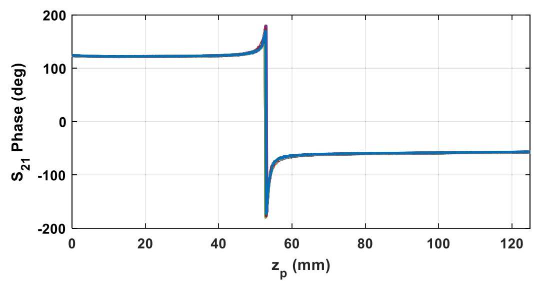

(b)

Fig. 14. Displacement sensor S_{21} measurement results from 50 measurement runs: (a) magnitude response and (b) phase response.

in Section IV, the probe was fixed at $(x_p, y_p) = (-4, 5 \text{ mm})$ to yield maximum sensitivity and least perturbation. The input port of the transmission line was connected to port 1 of the VNA, while the probe port was connected to port 2 of the VNA. Using a motorized precision positioner, the probe was then scanned along the length of the line from $z_p = 0$ to 125 mm with a step size of 0.2 mm. It is worth noting that the positioner incorporates the SFU1605 ball screw manufactured by TBI Motion Technology Company Ltd. This specific model has a C7 accuracy grade, delivering a remarkable positioning accuracy of ±0.05 mm across a 300-mm travel distance [58].

The VNA was used to measure the field around the transmission line by recording the complex S_{21} at every scan position. The scans were repeated 50 times to evaluate the repeatability of the sensor.

The measured magnitude and phase of S_{21} for all 50 measurement scans are shown in Fig. 14. The results show that the measurement is highly repeatable. The wavelength was estimated from the distance between the maximum and the minimum values of the measured $|S_{21}|$ for each measurement run. The mean value from the 50 runs is $\lambda_g = 221.1$ mm with a standard deviation of 3.056 mm. The mean estimated phase constant β is 28.43 rad/m with a standard deviation of 0.4 rad/m. These values compare well with the theoretical expectation for the used microstrip line ($\lambda_g = 221.5$ mm and $\beta = 28.36$ rad/m).

A. Concept Validation and Sensor Calibration

As described in Section II-C, the complex S_{21} measurement results of Fig. 14 can be fit to an ideal cosine function corresponding to the normalized magnetic field over the transmission line as given in (4), rewritten here for ease of accessibility. The null offset z_0 from the ideal cosine null position accounts for the probe offset from the reference position and ϕ_0, and the phase shift of the measured S_{21} at the position of $|S_{21}|_{\max}$ accounts for the input signal phase at the present measurement cycle

$$h_n\left(z_p\right) = e^{j\phi_0} \cos \beta \left(z_p - z_0\right). \tag{4}$$

The accuracy of an estimated displacement value can be negatively affected by the values of z_0 and ϕ_0. Therefore, to address this issue, measurements are typically carried out in two stages. The first stage is the calibration measurement, during which the initial phase and offset are determined. The second stage is the actual displacement measurement, in which these parameters are used to calculate the correction factors that improve the accuracy of the measurement. The calibration measurement step only needs to be performed once when the electronic unit of the sensor is first turned on. Subsequent displacement measurements can be taken with the same calibration data, allowing for increased efficiency and reducing the need for frequent recalibration.

The steps for obtaining the calibration parameters are highlighted in the following. First, the probe is positioned at $(x_p, y_p, 0)$. It is then solid in the z-direction from $z_p = 0$ to $z_p = 125$ at a step size of 0.2 mm. The VNA is used to measure complex S_{21} at every probe position. The measured S_{21} is normalized using $(S_{21}/|S_{21}|_{\max})$. The resulting normalized data S_c are used for computing the sensor parameters. If $z_{\max}$ and $z_{\min}$ represent the probe positions for $|S_c|_{\max}$ and $|S_c|_{\min}$, respectively, then z_0, λ_g, and β are computed as $z_0 = z_{\min}$, $\lambda_g = 4 \times (z_{\max} - z_{\min})$, and $\beta = (2\pi/\lambda_g)$, respectively. ϕ_0 is computed as the phase difference between $S_c(z_p)$ and an ideal cosine function $\cos(\beta z_p)$ at any z_p where $0 < z_p < 125$ mm.

To measure these parameters, one measurement run out of the 50 measurement runs set was used. The obtained values of the parameters are $\beta = 28.3$ rad/m, $z_0 = 2.7$ mm, and $\phi_0 = 121.46°$.

Fig. 15 shows the plot of the normalized values of the measured $|S_{21}|$ fit to the normalized ideal cosine function of (4). A very good match is obtained between the measured $|S_{21}|$ and the ideal cosine function within the range $20 < z_p < 125$ mm. As mentioned earlier, the response does not follow the sinusoidal distribution near the load due to the nature of the current distribution in space at that location.

B. Displacement Estimation

After obtaining the calibration parameters β, z_0, and ϕ_0, the probe displacement estimation was carried out. Equation (5), reproduced here for ease of accessibility, is utilized to estimate

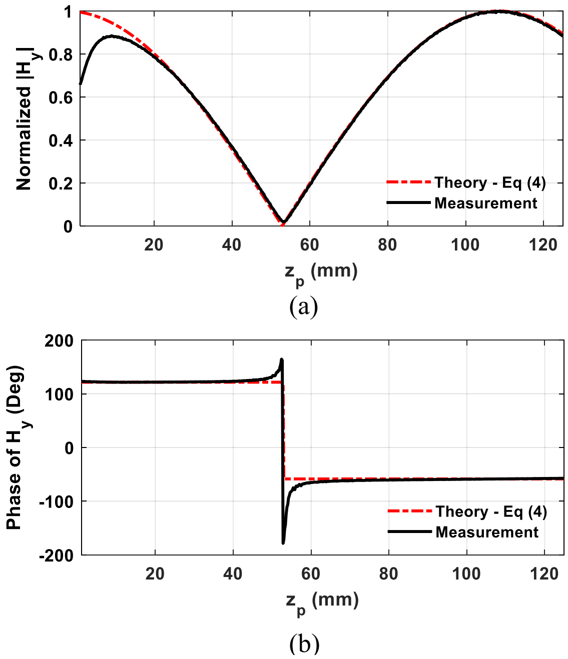

Fig. 15. Measured H-field variation along the z-axis using a VNA: (a) normalized magnitude variation and (b) phase variation.

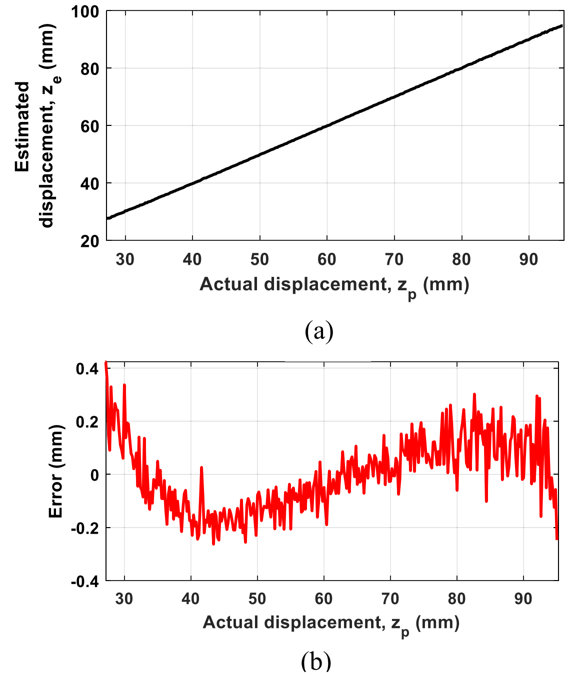

Fig. 16. Estimated probe displacement from the transmission line short position (a) within a range of 27–95 mm. (b) Estimation error within a range of 27–95 mm.

the displacement, where h_n is the normalized S_{21}. The estimation of the inverse cosine function is limited to the range of $z_p = 20$ mm to $z_p = 108$ mm. The point $z_p = 108$ mm corresponds to the point of maximum response. This limitation arises due to the ambiguity in resolving the measured response between the range $20 < z_p < 108$ mm, $z_p < 20$ mm, and $z_p > 108$ mm

$$z_e = z_0 + Re\left(\frac{\cos^{-1}\left(h_n e^{-j\phi_0}\right)}{\beta}\right). \tag{5}$$

Fig. 16(a) shows the estimated displacement values within the range $z_p = 27$–95 mm. The maximum estimation error within the range is within ± 0.45 mm, as shown in Fig. 16(b). The estimation error was calculated as follows:

$$\text{Error} = z_e - z_p \tag{6}$$

where z_e is the estimated probe displacement and z_p is the actual probe displacement (as determined from the precision positioning system).

To verify the repeatability of the measurement, the remaining 49 measurement runs were also used for displacement estimation but with the calibration parameters from the first measurement run. This is to demonstrate that multiple displacement measurements can be performed with a single calibration step. The average estimation error and the standard deviation of the estimation error are computed as (7) and (8), respectively, where n is the number of measurement runs

$$\overline{\text{Error}} = \frac{1}{n}\sum_{1}^{n} \text{Error}_i \tag{7}$$

$$\sigma = \sqrt{\frac{1}{n}\sum_{1}^{n}\left(\text{Error}_i - \overline{\text{Error}}\right)^2}. \tag{8}$$

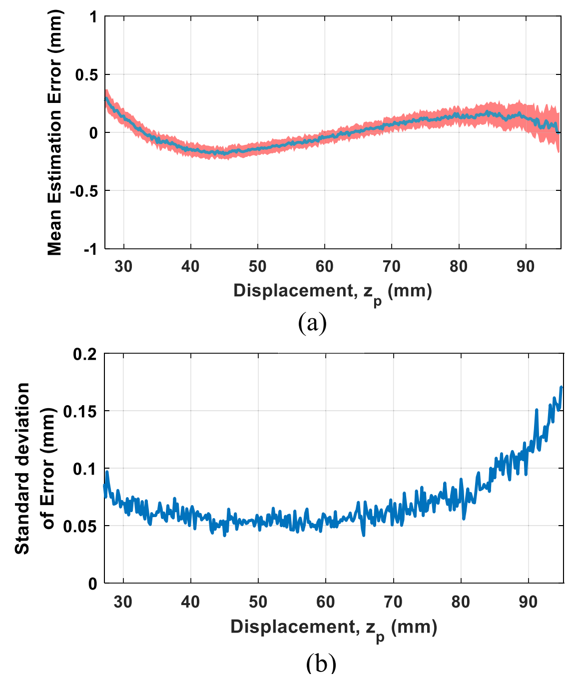

Fig. 17. Repeatability measurement results from 49 measurement runs of the sensor showing (a) error bar plot for the sensor within the range of 27–95 mm with the standard deviation interval highlighted and (b) standard deviation of the estimation error within the same range.

The estimated displacement error bar plot versus actual displacement for all 49 runs is plotted in Fig. 17(a). Within the range of $z_p = 27$–95 mm (68-mm range), the mean estimation error at any displacement point is less than ± 0.35 mm. Within the same range, the standard deviation of estimation error is less than 0.2 mm, as shown in Fig. 17(b). Overall, the

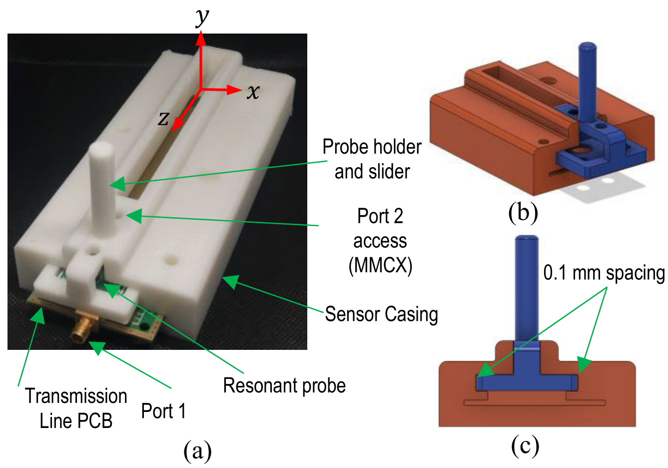

Fig. 18. (a) Photograph of the proposed linear displacement sensor in a 3-D-printed guiding structure, (b) perspective view, and (c) cross-sectional view of the 3-D model of the guiding structure and the probe holder and slider, showing that the slider is restricted to move in the z-direction only, thereby avoiding fluctuations in the x- and y-directions.

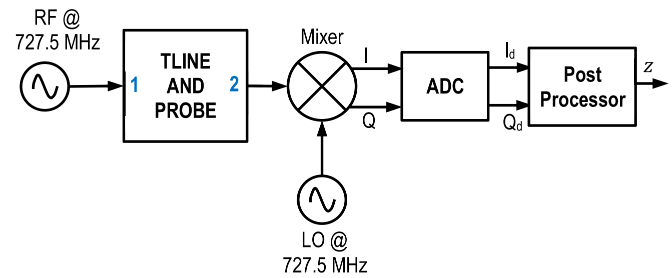

Fig. 19. Proposed architecture for the displacement sensor comprising the electronic circuitry for measuring the I and Q components of the coupling between the transmission line and the probe.

implemented system provides very accurate displacement estimation with a very low error (in the order of the positioner step size) with high repeatability/low uncertainty.

C. Enhancing Measurement Stability and Efficiency Through 3-D-Printed Guiding Structure

Fluctuations of the probe in the x- and y-direction can impact the sensitivity of the probe, as shown in Fig. 10, leading to measurement noise. To address this issue, the proposed sensor incorporates a 3-D-printed guiding structure that securely holds both the probe and the transmission line. As shown in Fig. 18(a)–(c), this structure restricts the probe's movement solely to the z-direction, effectively minimizing fluctuations in the x- and y-directions. The transmission line is fixed within the structure while the probe slides exclusively in the z-direction. During the design of the guiding structure and the probe holder, a clearance of 0.1 mm was allocated as the spacing between the guiding structure and the probe holder to ensure a smooth movement of the probe holder. As a result, fluctuations are confined within the narrow range of ± 0.1 mm. The measurement of magnetic field magnitude, as shown in the inset of Fig. 10, demonstrates that these fluctuations only yield a variation of 0.3%. The guiding structure was 3-D printed using polylactic acid + (PLA+) material with a relative permittivity, ε_r, ranging from 2.5 to 4.0 and a loss tangent ranging from 0.002 to 0.010 [59], [60].

In addition to minimizing fluctuations, the guiding structure also enhances measurement efficiency by preconfiguring the sensor with the probe positioned at $x_p = -4$ mm and $y_p = 5$ mm relative to the transmission line's short position in the xy plane.

D. Low-Cost Implementation of the Proposed Linear Displacement Sensor

Aside from the sensor being in a measurement-ready state with little or no setup required, real application displacement measurement also requires that the VNA should be replaced with a low-cost receiver circuitry that can measure the complex field coupling between the transmission line and the probe. Fig. 19 shows the proposed low-cost receiver architecture for on-the-field displacement measurement. It consists of two phase-locked oscillators, the transmission line and probe module (TLINE AND PROBE), an IQ mixer, an analog-to-digital converter (ADC), and a computer for postprocessing. The oscillators employed for testing purposes include the Keysight E8257D PSG signal generator and the N5181A MXG signal generator. The IQ mixer utilized is the Analog Devices LTC5584 IQ demodulator [61], renowned for its remarkable dynamic range that is perfectly suitable for the proposed sensor. To digitize the I and Q output signals generated by the mixer, the NI DAQ 9220 module was employed and operated at its maximum sampling rate of 100 kS/s. Subsequently, a combination of MATLAB and LabVIEW was utilized on a PC for the postprocessing stage.

The IQ mixer was characterized in a laboratory setup to assess its dynamic range and phase accuracy. This was carried out using the setup of Fig. 19 but without the TLINE AND PROBE. The RF signal directly feeds the RF port of the mixer. Fig. 20 shows the magnitude and phase response of the mixer as a function of the RF power level. The output power versus input power relationship is linear within the input power level of $P_{RF} = -75$ to -5 dBm [cf. Fig. 20(a)]. This 70-dB dynamic range is wide enough to accommodate the 42.3-dB dynamic range [cf. Fig. 12(a)] of the proposed sensor. Fig. 20(b) shows the phasor diagram as the phase of the input RF signal is varied from 0° to 360°. The perfect circular response suggests that the mixer has good phase accuracy.

The effectiveness of the proposed architecture in Fig. 19 for accurate displacement sensing was subsequently evaluated. To achieve this, a 727.5-MHz signal from the E8257D PSG signal generator was fed to Port 1 of the transmission line and probe module (input port of the transmission line). Port 2 of the module (input port of the probe) feeds the RF port of the IQ downconversion mixer. The mixer has a dynamic range greater than 70 dB with a maximum RF input signal of less than -5 dB. Consequently, the RF signal into port 1 was set to 12 dBm. To ensure that the coupled signal by the probe consistently remained within the linear range of the mixer and to facilitate impedance matching between the generator and the short-circuited transmission line, a 10-dB attenuator was connected at the generator's input port, thereby reducing the power level to an appropriate value. In addition, the local

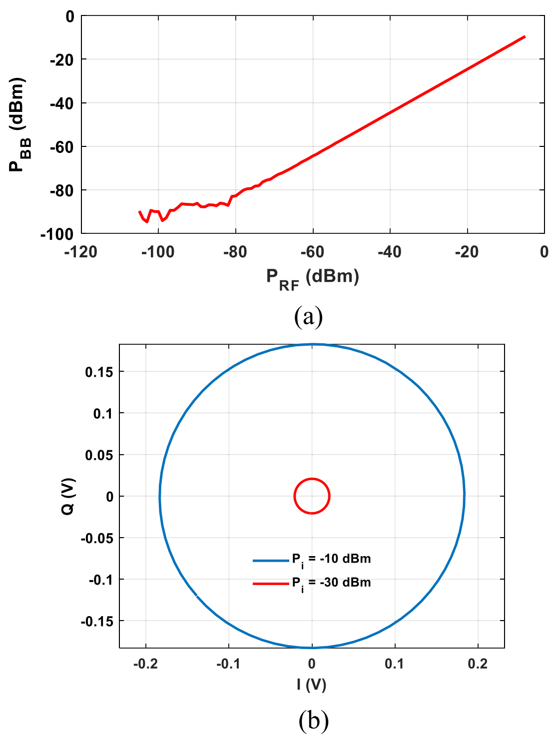

Fig. 20. (a) Measured magnitude response of the LTC 5584 *IQ* mixer (b) *IQ* phasor diagram for RF input phase variation.

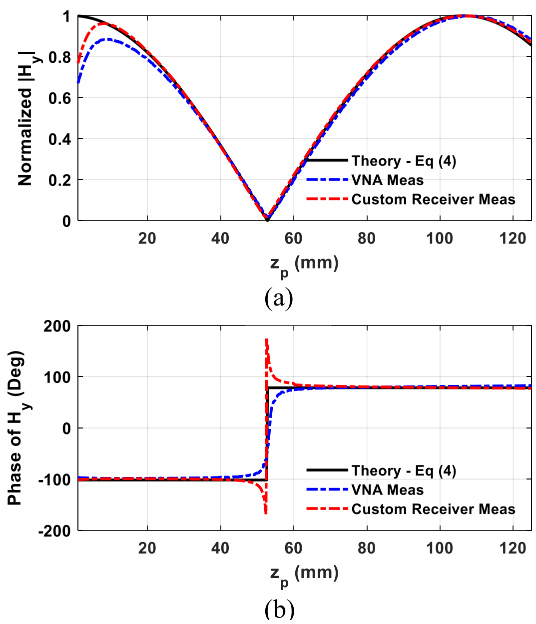

Fig. 21. Comparison between the custom receiver-based *IQ* measurement and the VNA S_{21} measurement (a) normalized magnitude variation and (b) phase variation.

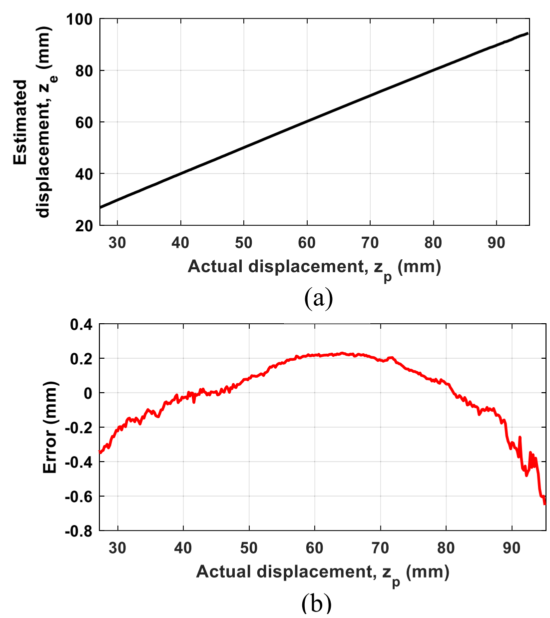

Fig. 22. Displacement estimation measurement results for the integrated sensor in a 3-D printed structure and using a low-cost electronic circuitry for data acquisition: (a) estimated probe displacement from the transmission line short position within the range of 27–95 mm and (b) estimation error within the range.

oscillator (LO) port of the mixer received a 727.5-MHz signal from the N5181A MXG signal generator. Furthermore, the oscillators were phase-locked to ensure synchronization and coherence.

In the integrated 3-D guiding structure shown in Fig. 18, the probe was scanned from $z_p = 0$ to $z_p = 125$ mm with a step size of 0.2 mm. The mixer I and Q output signals were acquired at every scan position. The digitized signals I_d and Q_d were then processed with a computer by combining them in the complex form to give the field coupling between the probe and the transmission line. This is the field distribution, $H_y(z_p)$, on the transmission line along the z-axis. The normalized magnitude of $H_y(z_p)$ is shown in Fig. 21(a). The VNA measurement response of Fig. 15 has been added for comparison. It is evident that the result is consistent with what was obtained using the VNA. The phase response is also shown in Fig. 21(b). This response is also consistent with what was obtained with the VNA in terms of the 180° phase shift at the null position. The actual phase angle is, however, different as the phase angle is a function of the reference plane, which is not necessarily the same for the two setups. For comparison purposes, the three-phase responses have been set to the same reference phase.

Using the proposed receiver and integrated sensor, the displacement was estimated within the range $z_p = 27$–95 mm, as reported in Fig. 22(a). The displacement estimation error over this range is plotted in Fig. 22(b). The obtained results are consistent with what was obtained with the VNA with only a slight increase in the estimation error.

For repeatability measurement, 50 measurement runs were carried out. To assess the impact of humidity on the sensor, ten of the 50 measurement runs were conducted without air conditioning, yielding a humidity range of 40−48%. The remaining 40 runs were performed with air conditioning, resulting in a humidity range of 50−60%. The sensor exhibited nearly identical responses under both humidity levels. Thus, the results from both conditions were combined for repeatability analysis.

The probe displacement was estimated and the displacement estimation error and the standard deviation of the estimation error are shown in Fig. 23. The standard deviation of the estimation error over the range $z_p = 27$ mm to $z_p = 95$ mm

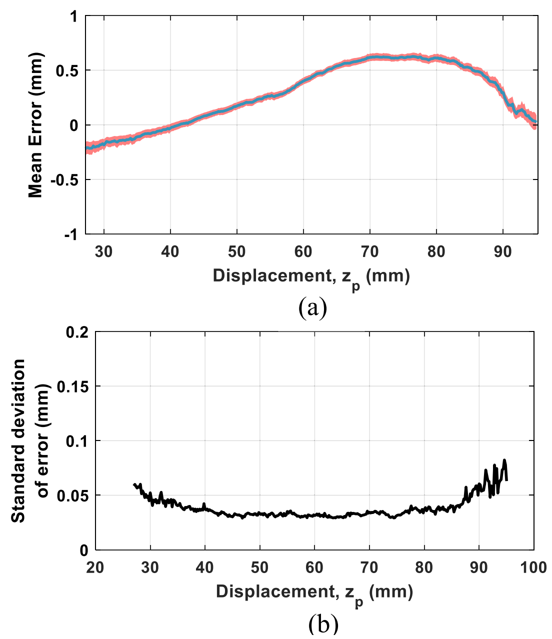

Fig. 23. Displacement estimation measurement results from 50 measurement runs for the integrated sensor in a 3-D printed structure and using low-cost electronic circuitry for data acquisition (a) estimation error within the range of 27–95 mm with standard deviation interval highlighted and (b) standard deviation of the estimation error within the range.

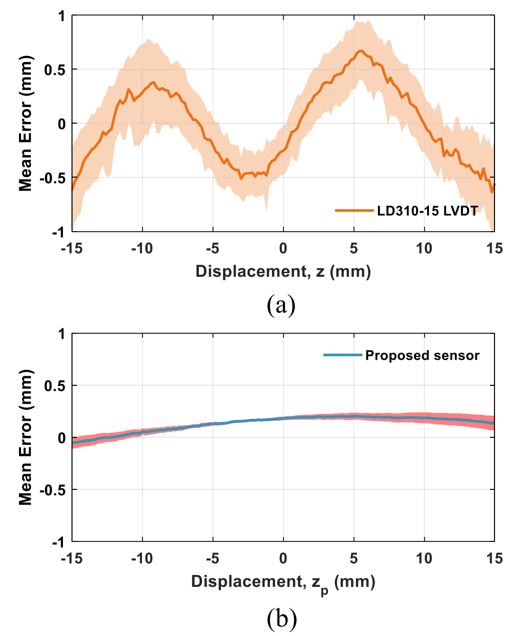

Fig. 24. Comparison of the displacement estimation error of the proposed sensor with that of the LD300-15 LVDT within a ±15-mm range (standard deviation interval is highlighted) using 15 measurement runs for both sensors: (a) mean displacement error of LD300-15 LVDT and (b) mean displacement error of the proposed sensor.

is less than 0.09 mm, while the mean displacement error within the range is less than 0.65 mm. For a reduced range of $z_p = 46$ mm to $z_p = 86$ mm, the standard estimation of error is less than 0.05 mm with the mean estimation error still within ±0.65 mm, as shown in Fig. 23(a) and (b). These results show that the measurements are highly repeatable with a measurement uncertainty of less than 0.09 mm.

The measurement errors of the proposed system can be attributed to the slight disparities between the parameters of the generated cosine function and the ideal cosine function of equal frequency. Such deviations occur due to the proximity of detected signal levels in the vicinity of the maximum $|H_y|$, i.e., at $z_p \cong 108$ mm [refer to Fig. 21(b)]. Consequently, the sensor exhibits reduced sensitivity within this range, thereby introducing variations in the estimated λ_g. Mitigating this issue calls for the design of a highly sensitive receiver capable of detecting small changes in signal amplitude within this region. Implementing such a receiver would effectively minimize the associated error.

VI. Comparison With State-of-the-Art

The proposed displacement sensor was compared to recently reported radio frequency-based linear displacement sensors, as summarized in Table I. It offers a maximum measurement range of 68 mm at 727.5 MHz with a measurement uncertainty of less than 0.09 mm, surpassing the capabilities of previously reported sensors [40], [41], [42], [43], [44], [46], [47], [48], [49], [50]. The proposed sensor's unique advantage lies in its scalability through operating frequency adjustment, allowing for customized dynamic range. In addition, unlike previous radio frequency-based sensors that only measure electrical quantities, the proposed sensor goes beyond this conventional approach by converting its measured electrical quantity (i.e., magnetic field coupling) into displacement, enabling accurate quantification of measurement uncertainty.

Although the proposed sensor exhibits a low sensitivity of 0.76 dB/mm at 727.5 MHz, it is optimized for a wide dynamic range. When compared to sensors based on similar principles, the proposed sensor demonstrates competitive sensitivity, outperforming other sensors by over 60 times in dynamic range [41], [46].

To further evaluate the performance of the proposed sensor, it was benchmarked against the industry-standard LD310-15 LVDT [62] with solartron OD4 inductive transducer signal conditioning electronics [63]. The LD310-15 LVDT has a dynamic range of ±15 mm and it was characterized following the similar procedure of calibration and measurement employed in this work. It was calibrated by varying the length of its spring-loaded rod from full extension to full compression in increments of 0.2 mm using the motorized positioner shown in Fig. 13. A linear curve fitting approach was employed to establish the relationship between the measured voltage and the displacement. The resulting linear curve parameters were subsequently utilized to estimate displacement in 14 additional measurement runs. The estimation error reported in Fig. 24 shows that the proposed linear displacement sensor has a comparable mean estimation error and low standard deviation of estimation error within a −15 to +15 mm range compared to the LVDT's estimation. A symmetrical bidirectional measurement range of ±15 mm was achieved for both sensors by adjusting the reference position to near the center of the sensors.

TABLE I
PERFORMANCE SUMMARY AND COMPARISON WITH OTHER RADIO FREQUENCY -BASED DISPLACEMENT SENSORS

Ref.	Year	Sensing Principle	Fixed or Variable Frequency ?	Operating Freq.	Size (mm × mm)	Dynamic Range (mm)	Average Displ. Estimation Error (mm)	Meas. Uncertainty (mm)	Sensitivity (dB/mm)	Converts measured quantity to displ.?
[43]	2020	Resonator - Tline Coupling	Fixed	3.69 GHz	NR	6	NR	NR	1.73	No
[40]	2022	Δf_o using $\lvert S_{11}\rvert$	Variable	1.3 - 1.98 GHz	NR	7	NR	NR	0.1 GHz/mm	No
[44]	2017	Δf of S_{21} TZ	Variable	3 – 5 GHz	0.03 λ_0^2	3	NR	NR	0.41 GHz/mm	No
[42]	2022	$\lvert S_{11}\rvert$	Fixed	3.34 GHz	19.4 ×3.2	8	NR	NR	3.5	No
[41]	2014	$\lvert S_{21}\rvert$	Fixed	4.253 GHz	NR	0.8	NR	NR	21.25	No
[46]	2013	$\lvert S_{21}\rvert$	Fixed	1.13 GHz	NR	1.1	NR	NR	23.5	No
[47]	2021	Phase of S_{21}	Fixed	13 GHz	NR	38	NR	NR	9.47°/mm	No
[48]	2020	Phase of S_{11}	Fixed	2 GHz	78 × 27	< 2	NR	NR	312.97°/mm	No
[49]	2022	Phase of S_{11}	Fixed	2.5 GHz	0.19 × 71.3^2	36	NR	NR	11°/mm	No
[50]	2004	Radar	Fixed	35.6 GHz	NR	4.25	0.027†	NR	84.7°/mm	Yes
This work	2023	Tline Magnetic field Coupling	Fixed	727.5 MHz	170 × 75	68	±0.65	0.09 (0.13 % FR)	0.76*	Yes
						40	±0.65	0.05 (0.13 % FR)	1.33*	
[62]	Bench mark sensor	LVDT	NA	0.4 – 10 kHz	245 × 20 (Cylindrical)	30	±0.6	0.4 (1.3 % FR)	16 mV/V/mm	Yes

†Maximum error | NR – Not reported | FR – Full range | NA: not applicable | *Average sensitivity over the stated dynamic range

In addition to accuracy, the proposed sensor offers cost-effective advantages. The *IQ* mixer is priced at \$15, while the printing of the guiding structure and fabrication of PCBs cost is less than \$20. In contrast, the LVDT is priced at \$375. Despite the LVDT's linear response, the proposed sensor eliminates the need for manual conversion and achieves direct displacement estimation through a postprocessor. Both sensors have similar structures and sizes dedicated to displacement measurement.

VII. CONCLUSION

This article presented a wide-range contactless radio frequency-based linear displacement sensor consisting primarily of a microstrip line and a nonperturbing probe to spatially map the magnetic field around the line. The sensing technique was analyzed thoroughly and the performance of the sensor was validated through extensive metrological characterization. Using a prototype operating at 727.5 MHz, it was demonstrated that the proposed sensor yields high overall measurement accuracy in a 68-mm range. Furthermore, the capability of the proposed sensor to provide accurate displacement measurements was benchmarked against a standard linear displacement sensor (i.e., LVDT). An application-ready and low-cost implementation of the sensor was also reported, discussed, and evaluated. The sensor yields the measurement uncertainty of less than 0.09 mm, which makes it suitable for critical positioning applications. The measurement range of the proposed sensor is scalable through the operating wavelength. Wider ranges could be realized by designing the sensor to operate at a lower frequency. The proposed method can also be used to design highly sensitive displacement sensors by using higher operating frequencies. It is remarked here that the results reported here were obtained without any error compensation. In the future, bias compensation techniques could be applied to further improve the accuracy.

REFERENCES

[1] J. Borenstein, H. R. Everett, L. Feng, and D. Wehe, "Mobile robot positioning: Sensors and techniques," *J. Robot. Syst.*, vol. 14, no. 4, pp. 231–249, Apr. 1997.

[2] S. Atiya and G. D. Hager, "Real-time vision-based robot localization," *IEEE Trans. Robot. Autom.*, vol. 9, no. 6, pp. 785–800, Dec. 1993.

[3] T. Laliberté and C. Gosselin, "Low-impedance displacement sensors for intuitive physical human–robot interaction: Motion guidance, design, and prototyping," *IEEE Trans. Robot.*, vol. 38, no. 3, pp. 1518–1530, Jun. 2022, doi: 10.1109/TRO.2021.3121610.

[4] T. Reininger, F. Welker, and M. Von Zeppelin, "Sensors in position control applications for industrial automation," *Sens. Actuators A, Phys.*, vol. 129, nos. 1–2, pp. 270–274, May 2006.

[5] A. Onat, C. Gurbuz, and S. Markon, "A new active position sensing method for ropeless elevator," *Mechatronics*, vol. 23, no. 2, pp. 182–189, Mar. 2013.

[6] S. J. Prosser, "Advances in sensors for aerospace applications," *Sens. Actuators A, Phys.*, vols. 37–38, pp. 128–134, Jun. 1993.

[7] J. Manwell, G. Bailey, P. Parsons, P. Richards, and D. Kreit, "An optical displacement transducer for aerospace applications," *Sens. Actuators*, vol. 18, nos. 3–4, pp. 233–237, Jul. 1989.

[8] R. W. Huggins, G. L. Abbas, C. S. Hong, G. E. Miller, C. R. Porter, and B. Van Deventer, "Fiber-coupled position sensors for aerospace applications," *Opt. Lasers Eng.*, vol. 16, nos. 2–3, pp. 79–103, Jan. 1992.

[9] B. Sun and B. Li, "Laser displacement sensor in the application of aero-engine blade measurement," *IEEE Sensors J.*, vol. 16, no. 5, pp. 1377–1384, Mar. 2016.

[10] K.-T. Park, S.-H. Kim, H.-S. Park, and K.-W. Lee, "The determination of bridge displacement using measured acceleration," *Eng. Struct.*, vol. 27, no. 3, pp. 371–378, Feb. 2005.

[11] J. Li, H. Hao, K. Fan, and J. Brownjohn, "Development and application of a relative displacement sensor for structural health monitoring of composite bridges," *Struct. Control Health Monitor.*, vol. 22, no. 4, pp. 726–742, Apr. 2015.

[12] W. N. MacPherson et al., "Tunnel monitoring using multicore fibre displacement sensor," *Meas. Sci. Technol.*, vol. 17, no. 5, pp. 1180–1185, May 2006.

[13] R. Gentner and J. Classen, “Development and evaluation of a low-cost sensor glove for assessment of human finger movements in neurophysiological settings,” *J. Neurosci. Methods*, vol. 178, no. 1, pp. 138–147, Mar. 2009.

[14] M. Borghetti, E. Sardini, and M. Serpelloni, “Sensorized glove for measuring hand finger flexion for rehabilitation purposes,” *IEEE Trans. Instrum. Meas.*, vol. 62, no. 12, pp. 3308–3314, Dec. 2013.

[15] K. Nizamis, N. Rijken, A. Mendes, M. Janssen, A. Bergsma, and B. Koopman, “A novel setup and protocol to measure the range of motion of the wrist and the hand,” *Sensors*, vol. 18, no. 10, p. 3230, Sep. 2018.

[16] S. Du, J. Hu, Y. Zhu, and M. Zhang, “An improved displacement measurement based on model reconstruction for permanent magnet synchronous motor,” *IEEE Trans. Instrum. Meas.*, vol. 66, no. 11, pp. 3044–3051, Nov. 2017.

[17] X. Zhou and Q. Yu, “Wide-range displacement sensor based on fiber-optic Fabry–Pérot interferometer for subnanometer measurement,” *IEEE Sensors J.*, vol. 11, no. 7, pp. 1602–1606, Jul. 2011.

[18] J. Kim, H. Chun, and C. Lee, “Three-axis displacement sensor-integrated spindle system for carbon fiber-reinforced plastic (CFRP) machining process monitoring,” *J. Manuf. Processes*, vol. 77, pp. 361–368, May 2022.

[19] Y. Fukuda, M. Q. Feng, Y. Narita, S. Kaneko, and T. Tanaka, “Vision-based displacement sensor for monitoring dynamic response using robust object search algorithm,” *IEEE Sensors J.*, vol. 13, no. 12, pp. 4725–4732, Dec. 2013.

[20] S. R. Lang, D. J. Ryan, and J. P. Bobis, “Position sensing using an optical potentiometer,” *IEEE Trans. Instrum. Meas.*, vol. 41, no. 6, pp. 902–905, Dec. 1992.

[21] M. F. Laguesse, “Optical potentiometer using fluorescent optical fiber for position measurement,” *Appl. Opt.*, vol. 28, no. 23, pp. 5144–5148, Dec. 1989.

[22] S. V. Thathachary, B. George, and V. J. Kumar, “A resistive potentiometric type transducer with contactless slide,” in *Proc. 7th Int. Conf. Sens. Technol. (ICST)*, Wellington, New Zealand, Dec. 2013, pp. 501–505.

[23] S.-T. Wu, S.-C. Mo, and B.-S. Wu, “An LVDT-based self-actuating displacement transducer,” *Sens. Actuators A, Phys.*, vol. 141, no. 2, pp. 558–564, Feb. 2008.

[24] H. Tariq et al., “The linear variable differential transformer (LVDT) position sensor for gravitational wave interferometer low-frequency controls,” *Nucl. Instrum. Methods Phys. Res. A, Accel. Spectrom. Detect. Assoc. Equip.*, vol. 489, nos. 1–3, pp. 570–576, Aug. 2002.

[25] F. Zhu, J. W. Spronck, and W. C. Heerens, “A simple capacitive displacement sensor,” *Sens. Actuators A, Phys.*, vol. 26, nos. 1–3, pp. 265–269, Mar. 1991.

[26] Y. Ye, C. Zhang, C. He, X. Wang, J. Huang, and J. Deng, “A review on applications of capacitive displacement sensing for capacitive proximity sensor,” *IEEE Access*, vol. 8, pp. 45325–45342, 2020.

[27] A. Babu and B. George, “Design and development of a new non-contact inductive displacement sensor,” *IEEE Sensors J.*, vol. 18, no. 3, pp. 976–984, Feb. 2018, doi: 10.1109/JSEN.2017.2780835.

[28] W. Gao, H. Shi, and Q. Tang, “A contactless planar inductive sensor for absolute angular displacement measurement,” *IEEE Access*, vol. 9, pp. 160878–160886, 2021, doi: 10.1109/ACCESS.2021.3131344.

[29] A. S. A. Kumar, B. George, and S. C. Mukhopadhyay, “An eddy current based non-contact displacement sensor,” in *Proc. IEEE Int. Instrum. Meas. Technol. Conf. (IMTC)*, Dubrovnik, Croatia, May 2020, pp. 1–6, doi: 10.1109/I2MTC43012.2020.9128506.

[30] A. Sun, Z. Wu, D. Fang, J. Zhang, and W. Wang, “Multimode interference-based fiber-optic ultrasonic sensor for non-contact displacement measurement,” *IEEE Sensors J.*, vol. 16, no. 14, pp. 5632–5635, Jul. 2016, doi: 10.1109/JSEN.2016.2569665.

[31] A. Missoffe, L. Chassagne, S. Topçu, P. Ruaux, B. Cagneau, and Y. Alayli, “New simple optical sensor: From nanometer resolution to centimeter displacement range,” *Sens. Actuators A, Phys.*, vol. 176, pp. 46–52, Apr. 2012.

[32] D. Ferrazzin, G. di Domizio, F. Salsedo, C. A. Avizzano, F. Tecchia, and M. Bergamasco, “Hall effect sensor-based linear transducer,” in *Proc. 8th IEEE Int. Workshop Robot Hum. Interact. (RO-MAN)*, Sep. 1999, pp. 219–224.

[33] G. Pepka, “Position and level sensing using Hall-effect sensing technology,” *Sensor Rev.*, vol. 27, no. 1, pp. 29–34, Jan. 2007.

[34] X. Song, J. Fang, and B. Han, “High-precision rotor position detection for high-speed surface PMSM drive based on linear Hall-effect sensors,” *IEEE Trans. Power Electron.*, vol. 31, no. 7, pp. 4720–4731, Jul. 2016.

[35] B. Morten, G. De Cicco, M. Prudenziati, A. Masoero, and G. Mihai, “Magnetoresistive thick film sensor for linear displacements,” *Sens. Actuators A, Phys.*, vol. 46, nos. 1–3, pp. 261–265, Jan. 1995.

[36] U. Dibbern, “Magnetic field sensors using the magnetoresistive effect,” *Sens. Actuators*, vol. 10, nos. 1–2, pp. 127–140, Sep. 1986.

[37] X. Li et al., “Magnetoresistive micro-displacement sensor based on magnetorheological fluid,” *Smart Mater. Struct.*, vol. 30, no. 4, Apr. 2021, Art. no. 045025.

[38] J. Mata-Contreras, C. Herrojo, and F. Martín, “Detecting the rotation direction in contactless angular velocity sensors implemented with rotors loaded with multiple chains of resonators,” *IEEE Sensors J.*, vol. 18, no. 17, pp. 7055–7065, Sep. 2018, doi: 10.1109/JSEN.2018.2853643.

[39] S. V. Thathachary, B. George, and V. J. Kumar, “Digital converter for a contactless displacement sensor,” *IEEE Trans. Instrum. Meas.*, vol. 64, no. 8, pp. 2155–2164, Aug. 2015, doi: 10.1109/TIM.2015.2390957.

[40] Z. Mehrjoo, A. Ebrahimi, and K. Ghorbani, “Microwave resonance-based reflective mode displacement sensor with wide dynamic range,” *IEEE Trans. Instrum. Meas.*, vol. 71, pp. 1–9, 2022, doi: 10.1109/TIM.2021.3130669.

[41] A. K. Horestani, J. Naqui, D. Abbott, C. Fumeaux, and F. Martín, “Two-dimensional displacement and alignment sensor based on reflection coefficients of open microstrip lines loaded with split ring resonators,” *Electron. Lett.*, vol. 50, no. 8, pp. 620–622, Apr. 2014.

[42] P. Regalla and A. V. P. Kumar, “A microwave dielectric resonator based sensor for detecting both linear and angular displacements,” in *Proc. Asia–Pacific Microw. Conf. (APMC)*, Nov. 2022, pp. 533–535.

[43] A. V. Praveen Kumar and P. Regalla, “A transmission mode dielectric resonator as a displacement sensor,” *IEEE Sensors J.*, vol. 20, no. 13, pp. 6979–6984, Jul. 2020, doi: 10.1109/JSEN.2020.2977893.

[44] M. Rezaee and M. Joodaki, “Two-dimensional displacement sensor based on CPW line loaded by defected ground structure with two separated transmission zeroes,” *IEEE Sensors J.*, vol. 17, no. 4, pp. 994–999, Feb. 2017, doi: 10.1109/JSEN.2016.2638859.

[45] C. Chio and K. Tam, “Microwave linear displacement and position sensor based on transversal signal interference,” in *Proc. Int. Conf. Microw. Millim. Wave Technol. (ICMMT)*, May 2021, pp. 1–3, doi: 10.1109/ICMMT52847.2021.9617876.

[46] A. K. Horestani, C. Fumeaux, S. F. Al-Sarawi, and D. Abbott, “Displacement sensor based on diamond-shaped tapered split ring resonator,” *IEEE Sensors J.*, vol. 13, no. 4, pp. 1153–1160, Apr. 2013.

[47] A. K. Horestani, Z. Shaterian, and M. Mrozowski, “High dynamic range microwave displacement and rotation sensors based on the phase of transmission in groove gap waveguide technology,” *IEEE Sensors J.*, vol. 22, no. 1, pp. 182–189, Jan. 2022, doi: 10.1109/JSEN.2021.3130658.

[48] J. Muñoz-Enano, P. Vélez, L. Su, M. Gil-Barba, and F. Martín, “A reflective-mode phase-variation displacement sensor,” *IEEE Access*, vol. 8, pp. 189565–189575, 2020, doi: 10.1109/ACCESS.2020.3031032.

[49] Z. Shaterian and M. Mrozowski, “Displacement sensors based on the phase of the reflection coefficient of a split ring resonator-loaded transmission line,” *IEEE Sensors J.*, vol. 22, no. 21, pp. 20321–20327, Nov. 2022, doi: 10.1109/JSEN.2022.3208435.

[50] S. Kim and C. Nguyen, “On the development of a multifunction millimeter-wave sensor for displacement sensing and low-velocity measurement,” *IEEE Trans. Microw. Theory Techn.*, vol. 52, no. 11, pp. 2503–2512, Nov. 2004.

[51] A. A. Mustapha, M. S. U. Rahman, and M. A. Abou-Khousa, “Polarimetric microwave sensor for angular speed measurement,” *IEEE Sensors J.*, vol. 22, no. 23, pp. 23145–23153, Dec. 2022, doi: 10.1109/JSEN.2022.3213174.

[52] M. A. Abou-Khousa, K. T. M. Shafi, and X. Xingyu, “High-resolution UHF near-field imaging probe,” *IEEE Trans. Instrum. Meas.*, vol. 67, no. 10, pp. 2353–2362, Oct. 2018, doi: 10.1109/TIM.2018.2815437.

[53] D. M. Pozar, *Microwave Engineering*. Hoboken, NJ, USA: Wiley, 2011, pp. 28–45.

[54] C. S. Suite. *Electromagnetic Field Simulation Software*. Accessed: May 2023. [Online]. Available: https://www.3ds.com/products-services/simulia/products/cst-studio-suite/

[55] E. J. Denlinger, “A frequency dependent solution for microstrip transmission lines,” *IEEE Trans. Microw. Theory Techn.*, vol. MTT-19, no. 1, pp. 30–39, Jan. 1971, doi: 10.1109/TMTT.1971.1127442.

[56] T. G. Bryant and J. A. Weiss, “Parameters of microstrip transmission lines and of coupled pairs of microstrip lines,” *IEEE Trans. Microw. Theory Techn.*, vol. MTT-16, no. 12, pp. 1021–1027, Dec. 1968, doi: 10.1109/TMTT.1968.1126858.

[57] A. Boyer, N. Nolhier, F. Caignet, and S. B. Dhia, "Closed-form expressions of electric and magnetic near-fields for the calibration of near-field probes," *IEEE Trans. Instrum. Meas.*, vol. 70, pp. 1–15, 2021, doi: 10.1109/TIM.2021.3126376.

[58] TBI Motion Technology. *Ball Screw Datasheet*. Accessed: Jun. 16, 2023. [Online]. Available: https://i0528.tbimotion.com.tw/storage/pdf/TBIMOTION_BallScrew_23.04(EN).pdf

[59] S. M. Lebedev, "A comparative study on thermal conductivity and permittivity of composites based on linear low-density polyethylene and poly(lactic acid) filled with hexagonal boron nitride," *Polym. Composites*, vol. 43, no. 1, pp. 111–117, Jan. 2022.

[60] J. Zechmeister and J. Lacik, "Complex relative permittivity measurement of selected 3D-printed materials up to 10 GHz," in *Proc. Conf. Microw. Techn. (COMITE)*, Apr. 2019, pp. 1–4.

[61] Analog Devices. *LTC5584—30 MHz to 1.4 GHz IQ Demodulator With IIP2 and DC Offset Control*. [Online]. Available: https://www.analog.com/media/en/technical-documentation/data-sheets/5584f.pdf

[62] Omega. *LD310 Series Spec Sheet*. Accessed: Feb. 26, 2023. [Online]. Available: https://br.omega.com/omegaFiles/pressure/pdf/LD310.pdf

[63] Solartron Metrology. *OD4 Datasheet*. Accessed: Jun. 16, 2023. [Online]. Available: https://solartron.cdistore.com/datasheets/solartron/od_family_en1.pdf

Ademola A. Mustapha (Member, IEEE) received the B.Sc. degree in electronic and electrical engineering from Obafemi Awolowo University, Nigeria, in 2008, and the M.Sc. degree in microsystems engineering and the Ph.D. degree in interdisciplinary engineering from the Khalifa University of Science and Technology, Abu Dhabi, UAE, in 2014 and 2018, respectively.

He worked as a Postdoctoral Fellow with the Center for Integrated Photonics and the Systems on Chip Center, Khalifa University of Science and Technology, from 2019 to 2021. During this period, he was involved in the design of high-speed and low-noise transceiver circuits and modules. He is currently working as a Postdoctoral Fellow at the Smart Sensing Systems (SSS) Group, Khalifa University of Science and Technology. His research interests include high-speed circuits and systems for communication and microwave-based sensors for nondestructive testing.

Omar S. Hassan received the B.Sc. degree (Hons.) in electrical engineering/communication from Ajman University, Fujairah, UAE, in 2015, and the M.S. degree in electrical and computer engineering from Khalifa University, Abu Dhabi, UAE, in 2022, with a research focus in antenna design, space communication, radio frequency (RF) measurement, and imaging.

He currently works as a Research Engineer with the Smart Sensing Systems (SSS) Group, Khalifa University. His research interests include antenna design and characterization, non-destructive testing, and microwave imaging.

Temesgen D. Ataro (Student Member, IEEE) is currently pursuing the bachelor's degree in electrical engineering from the Khalifa University of Science and Technology, Abu Dhabi, UAE.

In the Fall of 2022, he worked as an Undergraduate Research Assistant at the Smart Sensing Systems (SSS) Group, Khalifa University of Science and Technology, and during the Summer of 2023, he worked as an Intern at the Directed Energy Research Center, Division of the Technology Innovation Institute, Abu Dhabi, UAE.

Mr. Ataro is a member of the International Golden Key Honors Society for academic achievements in undergraduate studies.

Mohammed Saif Ur Rahman received the B.S. degree in instrumentation engineering from Osmania University, Hyderabad, India, in 2011, and the M.S. degree in control and instrumentation engineering from King Fahd University, Dhahran, Saudi Arabia, in 2015.

He is currently working as a Research Associate at the Smart Sensing Systems (SSS) Group, Khalifa University of Science and Technology, Abu Dhabi, UAE. His research interests include instrumentation, sensing systems, nondestructive testing, and microwave imaging.

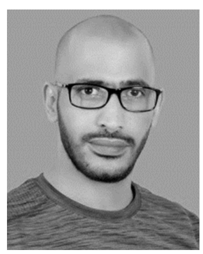

Mohamed A. Abou-Khousa (Senior Member, IEEE) received the B.S. (magna cum laude) degree from the American University of Sharjah, Sharjah, United Arab Emirates, in 2003, the M.S. degree from Concordia University, Montreal, QC, Canada, in 2004, and the Ph.D. degree from the Missouri University of Science and Technology (Missouri S&T), MO, USA, in 2009, all in electrical engineering (EE).

From 2005 to 2009, he was a Graduate Research Assistant with the Applied Microwave Nondestructive Testing Laboratory, Missouri S&T. He was a Research Scientist/Engineer at the Robarts Research Institute, London, ON, Canada, from 2009 to 2013. He is currently an Associate Professor with the Electrical Engineering and Computer Science Department, Khalifa University of Science and Technology, Abu Dhabi, UAE. His areas of expertise include radio frequency (RF), microwave, and millimeter-wave instrumentation, material characterization, nondestructive testing, and subsurface imaging. Over the course of his career, he executed various research and development projects within a broad range of sectors, including oil and gas, biomedical, space, and aerospace.

Dr. Abou-Khousa has coauthored many technical publications in his areas of expertise and has to his credit several patents. He was a recipient of multiple national and international awards, including the IEEE Instrumentation and Measurement Society 2017 Outstanding Young Engineer Award. As a coauthor, he was a recipient of the H. A. Wheeler Applications Prize Paper Award from the IEEE Antennas and Propagation Society. He serves as an Associate Editor-in-Chief for the IEEE TRANSACTIONS ON INSTRUMENTATION AND MEASUREMENT (TIM).